129 (2024) 205393

Contents lists available at ScienceDirect

Gas Science and Engineering

journal homepage: www.journals.elsevier.com/gas-science-and-engineering

Effects of stepwise depressurisation rate on methane hydrate dissociation dynamics at pore scale using microfluidic experiments

Junyu Yang [c], Qianghui Xu [a,**], Boyu Huang [a], Yizhe Liu [b], Zhiying Liu [b], Le Zhang [d], Kai H. Luo [c,*], Lin Shi [b]

[a] School of Mechanical Engineering, Beijing Institute of Technology, Beijing, 100081, China
[b] Key Laboratory for Thermal Science and Power Engineering of Ministry of Education, Department of Energy and Power Engineering, Tsinghua University, Beijing, 100084, China
[c] Department of Mechanical Engineering, University College London, Torrington Place, London, WC1E 7JE, United Kingdom
[d] Sinopec Petroleum Exploration & Production Research Institute, Beijing, 102206, China

ARTICLE INFO

Keywords:
Methane hydrate
Hydrate dissociation
Stepwise depressurisation
Pore scale
Microfluidic experiments

ABSTRACT

Methane hydrate, recognized as a potential alternative energy source, faces challenges in achieving efficient production. Stepwise depressurisation has emerged as a viable technique for enhancing productivity, yet optimizing the depressurisation rate remains a complex issue. This study employs pore-scale experiments using microfluidic chips to examine the dissociation characteristics of methane hydrate under varying stepwise depressurisation rates. At a high depressurisation rate of 0.4 MPa/15 min, the dissociation process exhibits a three-stage pattern: stabilisation, rapid dissociation, and slow dissociation. During these stages, the mass transfer limitation in the water phase significantly impedes the dissociation rate. The gas-water migration triggered by depressurisation can mitigate this limitation. As the depressurisation rate is reduced to 0.2 MPa/15 min, the rapid dissociation stage splits into two due to a decrease in gas-water migration intensity. The dissociation rate decreases by 45% compared to the 0.4 MPa/15 min case. This results from an insufficient driving force for dissociation, necessitating another depressurisation step. Further reduction of the depressurisation rate to 0.1 MPa/15 min leads to a less pronounced gas-water migration, which is inadequate to significantly counteract the mass transfer limitation. As a result, the rapid dissociation phase occurring at a depressurisation rate of 0.4 MPa/15 min, which exhibits an average dissociation rate of 0.2%/s, subsequently transitions into a more uniform and slower dissociation stage, where the average rate of dissociation declines to below 0.07%/s. The experimental results offer valuable insights for guiding hydrate exploration strategies during the stepwise depressurisation process by adjusting the depressurisation rate to regulate production.

1. Introduction

In view of the current climate change and energy shortages faced by the world, it is essential to find clean and efficient energy sources. Methane hydrates are considered a very promising alternative energy source due to their high storage capacity and abundant reserves (Sloan, 1998). Methane hydrates are crystalline compounds consisting of guest methane molecules encapsulated in the hydrogen-bonded water lattices by intermolecular forces (Sloan, 2003). Due to the low-temperature and high-pressure thermodynamic conditions required for stable formation, methane hydrates are widely distributed in deep-sea sediments (Wei et al., 2018) and terrestrial permafrost regions (Kan et al., 2021). In recent years, the exploitation of methane hydrates has received a lot of attention around the world (Anderson et al., 2011; Egorov et al., 2016; Liu et al., 2016; Chen et al., 2018; Yang et al., 2024a). Conventional extraction options for methane hydrates include depressurisation (Ji et al., 2001), thermal stimulation (Pang et al., 2009), inhibitor injection (Yuan et al., 2011), and gas replacement (Mok et al., 2022). These methods all contribute to the methane hydrates dissociation by altering the thermodynamic conditions of the reservoir to deviate from equilibrium. Among these exploitation methods, depressurisation has lower costs and higher efficiency, and is currently the most widely used.

* Corresponding author.
** Corresponding author.
E-mail addresses: xuqh12@bit.edu.cn (Q. Xu), k.luo@ucl.ac.uk (K.H. Luo).

https://doi.org/10.1016/j.jgsce.2024.205393
Received 27 February 2024; Received in revised form 13 May 2024; Accepted 27 June 2024
Available online 29 June 2024

During hydrate exploitation by depressurisation, the rate and magnitude of depressurisation are two key parameters. Depending on these two parameters, the depressurisation methods can be categorised into one-time rapid depressurisation, continuous slow depressurisation, stepwise depressurisation, and cyclic depressurisation (Yang et al., 2019). Compared to one-time rapid depressurisation, stepwise depressurisation can alleviate blockage problems caused by ice formation and hydrate reformation during hydrate dissociation, thus improving the productivity (Wang et al., 2018). In the stepwise depressurisation process, how to choose the appropriate depressurisation rate to achieve the optimal production efficiency is the key issue.

Methane hydrate dissociation is typically a multi-scale multi-physics problem (Yang et al., 2024a). During methane hydrate dissociation, a variety of complex mechanisms interact within the reservoir sediment pore structures to affect hydrate production performance, including multicomponent multiphase flow, conjugate heat transfer, species transport, intrinsic dissociation kinetics, and the microstructural evolution of sediments and hydrates. To find the best strategy for the stepwise depressurisation method, research has been carried out at multiple scales to understand the methane hydrate dissociation mechanisms during depressurisation. A review of previous field tests reveals the implementation of stepwise depressurisation in the 2008 Canada Mallik field test (Kurihara et al., 2010) and the 2017 Japan second Nankai Trough test (Yamamoto et al., 2019). In the Nankai Trough test, a two-stage depressurisation was employed, involving a reduction of bottle hole pressure from 13.0 MPa to 10.0 MPa in the first stage and 10.0 MPa–8.0 MPa in the second stage (Yamamoto et al., 2019). The 20-day fluid production showed no sand production issues. Turning attention to laboratory experiments, Gao et al. (2021) showed that, given the initial and final thermodynamic states, the depressurisation rate has little effect on gas and water recovery ratios. However, a reduced depressurisation rate, indicating an increase in depressurisation stages, limited the water production at each stage and enhanced the overall energy efficiency ratio. Similar findings related to the positive effect of the depressurisation rate on the exploitation efficiency were given by the numerical investigations (Ge et al., 2023).

The macroscale studies furnish theoretical guidance pertinent to the operational strategy of the stepwise depressurisation method. However, due to observational constraints, discerning the intricate processes occurring within the pore structure remains challenging. The nuanced multiphysical mechanisms governing methane hydrate dissociation within these structures are pivotal in determining the efficacy of stepwise depressurisation. A profound exploration of the sediment pore structure is imperative to comprehend these dissociation mechanisms thoroughly. Investigations at the pore-scale are capable of distinctly elucidating the phase transition and fluid flow attributes throughout the hydrate dissociation process, thereby aiding in understanding the dissociation mechanisms more comprehensively. Consequently, conducting studies at the pore scale is indispensable for enriching our understanding of the stepwise depressurisation method.

In the pore-scale study of methane hydrate dissociation, microfluidic chip is a common tool for the experimental investigation. Microfluidic chips, also known as lab-on-a-chip devices, are miniature devices used to manipulate and analyse small amounts of fluids with microscopic observation. This equipment enables in-situ observation of processes such as flow and phase transitions within microstructures with high spatial and temporal resolution. Pore-scale study on hydrates using microfluidic chips can date back more than 20 years, when Tohidi et al. (2001) observed the hydrate formation and dissociation in the glass microfluidic chip. Subsequently, microfluidic chips have been used more and more widely and proved to be an invaluable tool for unravelling the pore-scale dynamics of hydrate dissociation in two-dimensional pore structures. In response to depressurisation dissociation process, microfluidic chip-based studies can be traced back to the work of Katsuki et al. (2007). They observed that during the dissociation process, the generation of gas bubbles promoted further dissociation of the hydrate. The formation and subsequent growth of these small bubbles were attributed to the release of methane from methane-saturated water and gas expansion during depressurisation. Pandey et al. (2021) performed several experiments above and below 0 °C to understand the effect of hydrate morphology, distribution, local gas-fluid migration, and ice formation on the hydrate dissociation dynamics. Recently, Li et al. (2023) observed the hydrate dissociation in a micro-packed bed reactor and divided the dissociation into three stages: (1) pressure linearly decreased with no dissociation; (2) pressure hardly changed with some dissociation; (3) pressure nonlinearly decreased with complete dissociation. The aforementioned pore-scale studies afford an enhanced understanding of the dissociation mechanisms inherent to the depressurisation process. Existing research predominantly examines scenarios of one-time rapid depressurisation or continuous slow depressurisation, which focus on the evolutionary characteristics of hydrate dissociation. Within the context of stepwise depressurisation, the rate and magnitude of depressurisation emerge as critical determinants of its properties. Comprehending the evolutionary dynamics of hydrates during depressurisation, as well as elucidating the interplay between depressurisation rate and magnitude, are pivotal for guiding practical extraction processes. Nonetheless, investigations into stepwise depressurisation remain markedly scant. Moreover, even fewer studies have delved into the interrelations between the depressurisation rate and dissociation characteristics, which are crucial for understanding the mechanisms underlying stepwise depressurisation. Concurrently, prevailing research predominantly emphasises qualitative phenomena of hydrate dissociation, with quantitative explorations into hydrate dissociation rates remaining notably scarce. Given that quantitative analyses are pivotal in accurately assessing the efficacy of various depressurisation strategies, there remains a critical need for more comprehensive and rigorous studies in this domain.

Given the notable absence of pore-scale experimental investigations into stepwise depressurisation, this study pioneers the examination of methane hydrate dissociation using a high-pressure microfluidic chip during a stepwise depressurisation process. By meticulously identifying the mechanisms of methane hydrate dissociation at various depressurisation rates, this work elucidates their consequential impacts on dissociation efficacy. Beyond merely observing experimental phenomena, this work innovatively applies image segmentation techniques to experimental images, enabling quantification of the hydrate dissociation rate to obtain a fuller understanding of the effects of depressurisation rates. The novel insights derived from these methodological advancements provide crucial empirical guidance for optimizing the stepwise depressurisation recovery process.

2. Experimental section

2.1. Materials

In the present work, a microfluidic chip simulating the rock structure manufactured by Micronit Microfluidics BV in the Netherlands was used to investigate the methane hydrate dissociation process with stepwise depressurisation processes, as shown in Figure S1(a). The pore structure within the chips is generated through an etching process. This process involves exposing a piece of glass to acids that dissolve the glass, while a mask covers specific areas, resulting in the desired pore structure. The chip has a size of 45 mm × 15 mm, a permeability of 2.5 Darcy, and can withstand an internal pressure of up to 10 MPa high-purity methane gas (Beijing Praxair Inc, 99.99%) and deionized water (Zhejiang Nandai Inc) were injected into the microfluidic chip to produce methane hydrates. To facilitate the fluid injection and production, two nanoports with nanotubing guiders were strategically positioned at each side of the microfluidic chip.

2.2. Experimental apparatus

The schematic diagram of the experimental system is shown in Figure S1(b), which is improved from our previous work (Yang et al., 2024b). The microfluidic chip is fixed on a copper holder and immersed into a cryogenic environment chamber. The cryogenic chamber is composed of the inner and outer layers, both filled with ethylene glycol antifreeze. The inner layer is transparent and left to stand for better observation; the outer layer is filled with glycol antifreeze through a cryogenic water bath. The outer layer of liquid is continuously circulated through a cryogenic water bath to control the temperature of the microfluidic chip and its surrounding environment. The temperature control range of the water bath is 253.15–303.15 K. The inner and outer chambers were separated by the copper wall for uniform and rapid heat transfer, enabling the effective temperature control of the inner chamber.

Deionized water is administered into the microfluidic chip employing a plunger pump (Beijing Xingda Science and Technology Development Co., 2 ZB-2L20A, up to 20 MPa), while methane gas is introduced via a high-pressure cylinder. This injection procedure is meticulously regulated by a mass flow controller (Brooks SLA5850), which offers a control range of 0–3 mL/min and an accuracy of 0.6%, operating within a pressure range of 0.1–10.3 MPa. This method facilitates internal chip pressurization through the introduction of water or gas. Pressure transducers (Yokogawa EJA510E) situated at both the entrance and exit of the micromodel provide measurements of injection and production pressure. Concurrently, thermal resistances (Heraeus PT100) positioned directly beneath the micromodel register the temperature. The hydrate generation and dissociation process within the microfluidic chip are observed and documented using a high-resolution microscope (Olympus STM6) and an affiliated top-mounted microscope camera (Nikon DS-Fi3), achieving a spatial resolution of approximately 0.38 μm/pixel with 10 × objective lenses and a temporal resolution of 2 frames/s. An automatic backpressure regulator (Ocean CENT, BP-A3000, up to 20 MPa) is integrated to manipulate the micromodel pressure accurately to the designated target, maintaining a pressure uncertainty of ±1%. The adjustment of the backpressure valve enables the execution of a stepwise depressurisation process, accommodating varying rates of pressure reduction.

2.3. Experimental procedure

To examine the stepwise depressurisation process, it is pivotal to initiate with a pertinent hydrate distribution within the microfluidic chip. In this study, each experimental run was instigated with methane formation at 275.15 K and a pressure of 3.2 MPa. Following the successful completion of the leak check and evacuation procedures, the microfluidic chip was saturated with deionized water, maintaining a constant flow rate of 3.3 mL/min and atmospheric outlet pressure. Subsequently, the backpressure valve was modulated to 3.2 MPa, allowing continuous methane gas injection into the chip. During this stage, the pressure experienced a gradual increment, displacing a segment of the water. The gas injection was halted once the chip pressure attained 3.2 MPa and the gas-water distribution within the chip was deemed optimal. Thereafter, the water bath was activated to lower the system temperature to 253.15 K, leading to the freezing of the internal water phase of the chip. The system temperature was then elevated to 277.15 K to melt the ice phase. The nuclei, engendered by the water's ablation post-freezing, serve as facilitators for swift hydrate formation (Li et al., 2023). Eventually, the temperature was reduced again to 274.15 K to trigger hydrate formation and maintained the methene hydrate stability condition for approximately 2 h. Since the equilibrium pressure at 274.15 K is about 2.9 MPa, the pressure-temperature conditions at this point are sufficient to ensure the stable existence of the methane hydrate.

After generating the methane hydrate in the microfluidic chip, the valve at the chip inlet was closed, and the stepwise depressurisation was achieved by the automatic backpressure valve at the constant temperature of 274.15 K. Different depressurisation rate was adopted to investigate the dissociation mechanisms. The time interval between each depressurisation operation was 15 min for all the cases and the magnitude of each drop was different to achieve different depressurisation rate. Three depressurisation magnitudes were adopted in the experiments, including 0.1 MPa, 0.2 MPa, and 0.4 MPa. Each set of experiments was repeated three times to ensure the generalisability of the mechanism understanding (Test 1, 2, 3 for each set). During the depressurisation process, the microscope camera remained in operation to monitor and record the phase change process in the microfluidic chip. When the pressure inside the chip decreased to 2.0 MPa, the recording was stopped.

After capturing the experimental images, the images underwent segmentation to delineate the phase change pattern and quantify the hydrate dissociation rate, as delineated in Figure S2. Four phases were identified in the chip as shown in Figure S2(a), including the glass matrix (GM), water (W), gas (G) and hydrate (H). Similar to the previous work (Almenningen et al., 2018), two distinct hydrate morphologies were observed, namely the hydrate film and hydrate crystal. The two forms of hydrate were recognisable as they refract and reflect light differently and thus took on different colours. The hydrate films were porous hydrate shells with encapsulated gas, appearing as dark brown, while the hydrate crystals were nonporous crystalline hydrates, showing bright brown colour. In this paper, the volume occupied by both hydrate morphology was included in the calculation of hydrate saturation. The segmentation utilized the ilastik toolkit (Berg et al., 2019), employing interactive machine learning algorithms. Due to the unchanging matrix structure of the microfluidic chip during dissociation and the similarity in pixel characteristics of the glass matrix and water, which hindered segmentation accuracy, the matrix structure was first extracted to create a mask. In the subsequent experimental images, only the water, gas and hydrate phases need to be distinguished. After generating the mask, a set of representative pixels from the raw microscopic image were manually labelled as water, gas and hydrate. A machine learning model, based on the random forest approach, was then trained. This model assigns labels to pixels based on features like colour, texture, and shape, in tandem with manual annotations. The labelling-training-prediction workflow was iteratively conducted to refine the classification until achieving the desired segmentation accuracy. The exported classifier model was then applied to the experimental images at different times to obtain a series of segmented images. Based on the segmented image, we can count the number of pixels in each phase N_i and thus calculate the saturation of each phase S_i at different dissociation time t by

$$S_i(t) = \frac{N_i(t)}{N_{\text{total}} - N_{\text{GM}}}, i = \text{W}, \text{G}, \text{H} \tag{1}$$

where. N_{total}. is the total pixel count within the microscopic image, and N_{GM} the pixel count belonging to the micromodel glass matrix. Based on the hydrate saturation at different time point, the hydrate dissociation rate R can be calculated by the difference between the results of two experiments within a time interval Δt as

$$R(t) = \frac{S_{\text{H}}(t + \Delta t) - S_{\text{H}}(t)}{\Delta t} \tag{2}$$

The above calculation facilitated the derivation of dissociation rate curves under varying stepwise depressurisation conditions, enabling a detailed analysis of the effects of depressurisation rates.

3. Results and discussions

3.1. Hydrate dissociation characteristics during stepwise depressurisation

The experimental condition characterized by a depressurisation rate

of 0.4 MPa/15 min was firstly utilized to elucidate the dissociation characteristics inherent in stepwise depressurisation. The depressuration rate is selected according to the previous research (Li et al., 2023). Fig. 1 delineates the temporal variation in hydrate residual ratios across three experimental sets. The hydrate residual ratio is quantified as the proportion of the residual hydrate saturation relative to the initial saturation throughout the dissociation sequence. Concurrently, Fig. 2 shows the varying rates of hydrate dissociation at distinct temporal junctures corresponding to these experiments. A careful examination of Figs. 1 and 2 reveals that the hydrate dissociation transpires in three discernible phases: initially, the hydrate stabilisation stage ($t = 0 - 900$ s) marked by a negligible dissociation rate—so minimal that instances of hydrate formation and an uptick in the residual rate are noted, with an average dissociation rate of 9.87×10^{-3} %/s; subsequently, the rapid hydrate dissociation stage ($t = 900 - 1200$ s), characterized by a notably higher average dissociation rate of 0.2%/s; and finally, the slow hydrate dissociation stage ($t = 1200 - 2700$ s), where the dissociation proceeds at a reduced average rate of 1.40×10^{-2} %/s. Subsequent sections will delve into a detailed analysis of the unique dissociation characteristics and underlying causes of each stage, drawing upon data from the experimental imagery.

3.1.1. Stabilisation stage

Fig. 3 illustrates a representative image from Test 1 at 0.4 MPa/15 min, capturing the hydrate stabilisation stage ($t = 0 - 900$ s) to elucidate dissociation characteristics. Initially, the chip outlet pressure diminishes from 3.2 MPa to 2.8 MPa at $t = 0$ s, slightly lower than the equilibrium pressure 2.9 MPa. This pressure gradient across the chip instigates the migration of gas and water phases within the flow channel, resulting in a notable alteration of the gas-water distribution. Specifically, certain regions exhibit a transition from a gas-dominant to a water-dominant phase, as shown in Fig. 3 at $t = 300$ s. Subsequently, equilibrium is attained between the chip inlet and outlet pressures, halting further gas-water migration. This equilibrium state and the unaltered gas-water distribution are distinctly visible in Fig. 3 at both 300 s and 900 s. Throughout the experiment, despite minor localized hydrate formation and dissociation events, the overall structure of the hydrate crystals demonstrates notable stability. This stability is further corroborated by the near-constant hydrate saturation levels and the maintenance of the hydrate residual rate at approximately 1.0, as depicted in Fig. 1.

To gain deeper insights into the evolutionary pattern of hydrates at this stage, a detailed analysis of locally enlarged experimental images is conducted, as illustrated in Fig. 4. During the initial phase of depressurisation ($t = 0 - 300$ s), the pressure difference between the inlet and outlet initiates gas-water migration, leading to a minor dissociation of

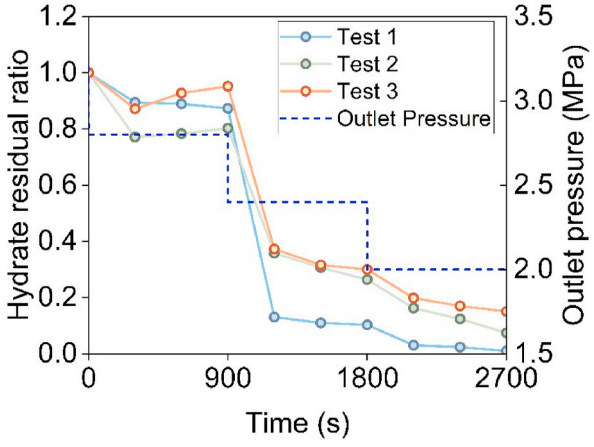

Fig. 1. Hydrate residual rate curves for different experimental tests with the depressurisation rate of 0.4 MPa/15 min.

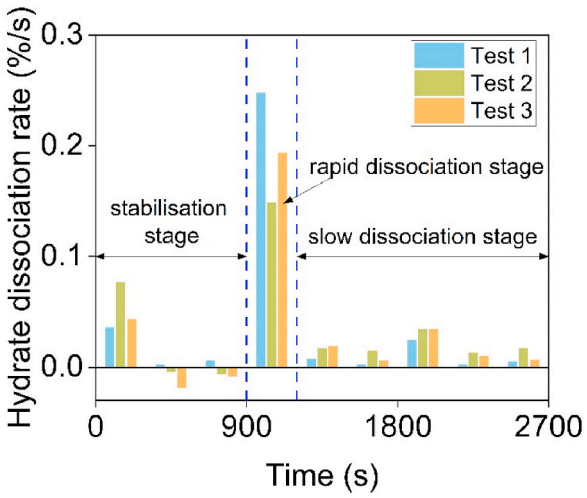

Fig. 2. Average hydrate dissociation rate during different time intervals for different experimental tests with the depressurisation rate of 0.4 MPa/15 min. Three dissociation stages are identified.

the hydrate film, as depicted in Fig. 4(a). This hydrate film, being relatively thin, disintegrates swiftly within a 300-s timeframe. Concurrently, a portion of the hydrate film remains intact due to water seepage. Owing to the hydrophilic nature of hydrates, the influx of water results in the displacement of the gas phase previously encapsulated within the hydrate film by the water phase. Consequently, the hydrate film undergoes a noticeable colour shift, attributed to alterations in light refraction and reflection caused by the water intrusion, although no substantial dissociation is observed.

When the pressure inside the chip is stabilised after $t = 300$ s, gas-water migration stops. Subsequently, a gradual reduction in the volume of bubbles within the local water phase is noted, coinciding with the in-situ formation of a limited quantity of hydrate crystals, as depicted in Fig. 4(b). The emergence of these hydrate crystals suggests that the local pressure conditions persistently exceed the phase equilibrium threshold. It is evident that during the hydrate stabilisation stage, despite a rapid decrease in pressure along the main flow path due to a reduction in outlet pressure, the pressure in regions not aligned with the main flow path declines more gradually, maintaining a relatively high level. Moreover, the observed hydrate crystal formation is accompanied by a minor degree of hydrate dissociation, as illustrated in Fig. 4(c). This dissociation is inferred from the observed increase in the volume of bubbles encased by hydrate crystals.

Although localized instances of hydrate synthesis and dissociation have been observed, the bulk of the hydrate structure remains largely unaltered as shown in Fig. 3. This phenomenon can be primarily attributed to a conjunction of two key factors. Firstly, the disparity between the chip pressure, at 2.8 MPa, and the equilibrium pressure, at 2.9 MPa, is minimal, thereby offering an insufficient thermodynamic driving force for dissociation. Secondly, the impediment to mass transfer within the water phase significantly curtails the rate of hydrate dissociation. The extensive water phase surrounding the hydrate crystals acts as a kinetic barrier, effectively isolating them from the gas phase(Yang et al., 2023). This isolation impedes the mass transfer rate between the gas and water phases. Consequently, this hampers the swift migration of methane molecules towards the main flow path, leading to an increase in local fugacity f_h. Based on the widely recognized Kim-Bishnoi model (Kim et al., 1987), the hydrate dissociation rate $\dot{r}$ is determined by

$$\dot{r} = -k \exp\left(\frac{E_a}{RT}\right) A \left(f_{eq} - f_h\right) \tag{3}$$

where k, E_a, R and A are the pre-exponential factor, activation energy, gas constant and hydrate surface area, respectively. The high local

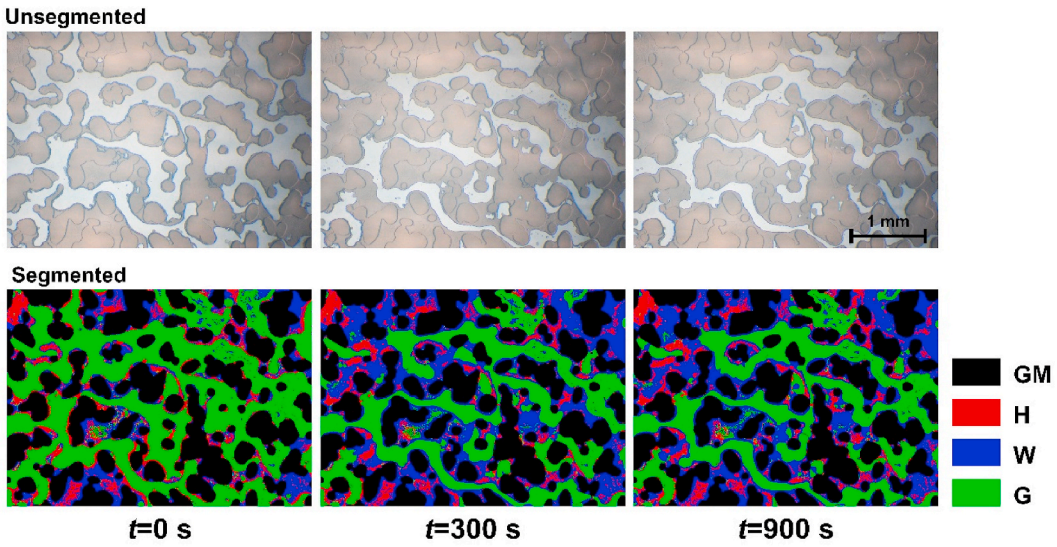

Fig. 3. Experimental snapshot and segmented images during stabilisation stage of Test 1 with a depressurisation rate of 0.4 MPa/15 min.

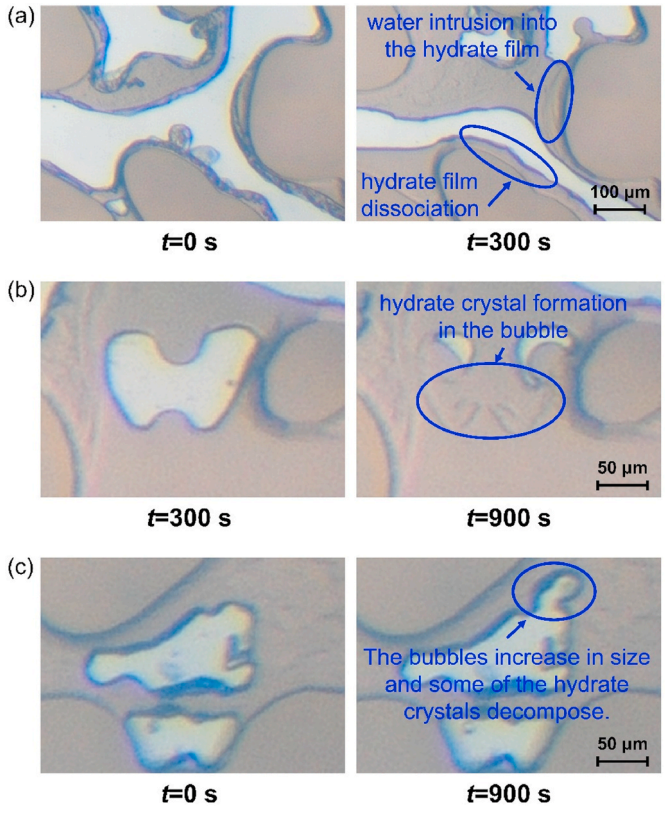

Fig. 4. Local magnification of the experimental snapshot during stabilisation stage from (a) Test 3, (b) Test 1, (c) Test 1 with a depressurisation rate of 0.4 MPa/15 min.

fugacity lowered the dissociation drive $\left(f_{eq} - f_h\right)$, consequently decelerating the hydrate dissociation. These two factors collectively contribute to a notable reduction in the rate of hydrate dissociation during the stabilisation stage.

3.1.2. Rapid dissociation stage

Following the stabilisation stage, hydrate in the chip experiences a rapid dissociation within $t = 900 - 1200$ s. Fig. 5 shows the typical characteristics of the rapid dissociation stage from Test 3 experiment. When the chip outlet pressure decreases from 2.8 MPa to 2.4 MPa at $t = 900$ s, the pressure difference between the inlet and outlet triggers intense gas-water migration, accompanied by the rapid dissociation of hydrate film and hydrate crystals ($t = 905$ s). The hydrate dissociation is mainly focused in the vicinity of the main flow channel in the gas phase. Subsequently, the local bubbles enclosed in the water and hydrate phases increase rapidly in size ($t = 1200$ s), with some coalescing to form new flow channels ($t = 960$ s). The emergence of these channels further amplifies the area affected by rapid hydrate dissociation, ultimately leading to the dissociation of most of the hydrate content in the chip.

The rapid hydrate dissociation results from a combination of pressure reduction and gas-water migration. As delineated in Eq. (3), the fugacity of methane at the hydrate surface is a key driver in determining the hydrate dissociation rate. When the pressure decreases, the solubility of methane molecules in the water phase decreases and some supersaturated methane molecules escape from the water phase. At the same time, the gas-water migration can lessen the thickness of the water layer enveloping the hydrate crystals as shown in Fig. 6. This reduction enables direct contact between some hydrate crystals and the low-pressure gas phase, thereby diminishing mass transfer resistance in the water phase. As a result, methane molecules released from the dissociation reaction can migrate to the gas phase more rapidly. Subsequently, the methane concentration in the water phase at the hydrate surface decreases, enhancing the driving force for hydrate dissociation. The growth and interconnection of bubbles further augment the gas-water migration effect. As plotted in Fig. 2, during $t = 1200 - 1800$ s, the hydrate dissociation rate is very slow compared to that of $t = 900 - 1200$ s, although the pressure remains as low as 2.4 MPa. During this phase, the fluid in the chip is relatively stable, exhibiting minimal migration, and the facilitative effect of gas-water migration is less pronounced. This observation underscores the significance of gas-water transport as a critical factor in accelerating the rate of hydrate dissociation.

3.1.3. Slow dissociation stage

As previously discussed, during the latter phase of rapid dissociation, a state of equilibrium is achieved between the inlet and outlet pressures, resulting in the cessation of gas-water migration and a transition of hydrate dissociation into the slow dissociation stage, characterized by a marked reduction in the dissociation rate. Fig. 7 exemplifies this slow dissociation phase as observed in Test 3. At the end of the rapid

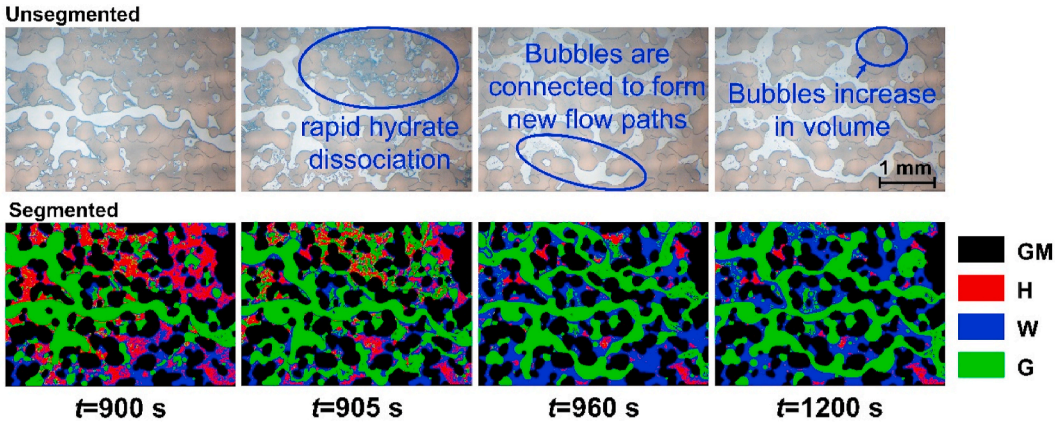

Fig. 5. Experimental snapshots and segmented images during rapid dissociation stage of Test 3 with depressurisation rate of 0.4 MPa/15 min.

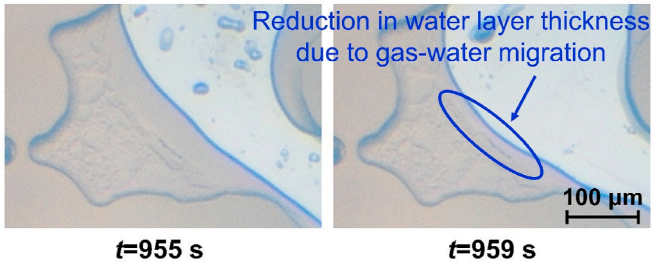

Fig. 6. Local magnification of the experimental snapshot during rapid dissociation stage from Test 1 with depressurisation rate of 0.4 MPa/15 min.

dissociation stage (t = 1200 − 1800 s), a residual quantity of hydrate, predominantly localized within the pore throat structures which are less accessible to the gas phase and encased in the water phase, remains within the chip. The dissociation rate is predominantly constrained by the mass transfer limitations within the water phase, as previously mentioned. The enlarged local view in Fig. 8 reveals that, between 1200 and 1800 s, the dissociation rate of hydrates enveloped by the water layer is notably sluggish, primarily due to these mass transfer limitations. At t = 1800 s, the outlet pressure decreases from 2.4 MPa to 2.0 MPa, which reinitiates intense gas-water migration. This change facilitates the gas phase invasion of pore throat structures, consequently diminishing the mass transfer resistance and enabling rapid hydrate dissociation in these regions, as illustrated in Fig. 8(a) at t = 2100 s. Additionally, the accelerated gas flow also reduces the thickness of water layers on the hydrate surface, further alleviating the mass transfer limitations of the water layers, as depicted in Fig. 8(b) at t = 2100 s. These changes result in some enhancement of the hydrate dissociation rate, which is reflected in the increase observed at t = 1800 − 2100 s in Fig. 2.

After t = 2100 s, as shown in Fig. 7, most hydrate within the chip undergoes dissociation, resulting in a reduced surface area of the hydrate. Concurrently, the fluid dynamics within the chip approach a state of equilibrium. This stabilisation leads to the cessation of gas-water migration, thereby diminishing the facilitating effect on hydrate dissociation. These combined factors contribute to a markedly reduced rate of hydrate dissociation during the final stage of the stepwise depressurisation process.

In summary, the distinct characteristics of the three phases observed in the hydrate dissociation process with the stepwise depressurisation rate of 0.4 MPa/15 min have been comprehensively recognized. From the analysis of these stages, it becomes evident that the dynamics of gas-water migration, as influenced by the depressurisation in each step, are pivotal in determining the rate of hydrate dissociation.

3.2. *Effects of stepwise depressurisation rate*

Upon identifying the segmented characteristics inherent in a typical stepwise depressurisation process at a rate of 0.4 MPa/15 min, various depressurisation rates are employed to examine their impact on hydrate dissociation. Fig. 9 shows the experimental results of hydrate dissociation with the stepwise depressurisation rate of 0.2 MPa/15 min. The hydrate residual ratio curves depicted in Fig. 9(a) reveal that the pattern of change in the hydrate dissociation rate also exhibits a segmented characteristic. However, in contrast to the condition of 0.4 MPa/15 min, the rapid hydrate dissociation stage is divided into two distinct stages.

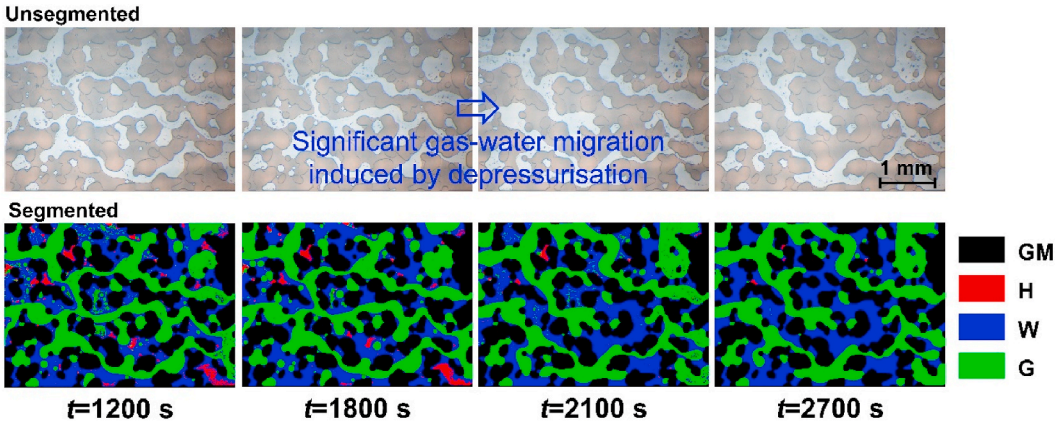

Fig. 7. Experimental snapshots and segmented images during slow dissociation stage of Test 3 with depressurisation rate of 0.4 MPa/15 min.

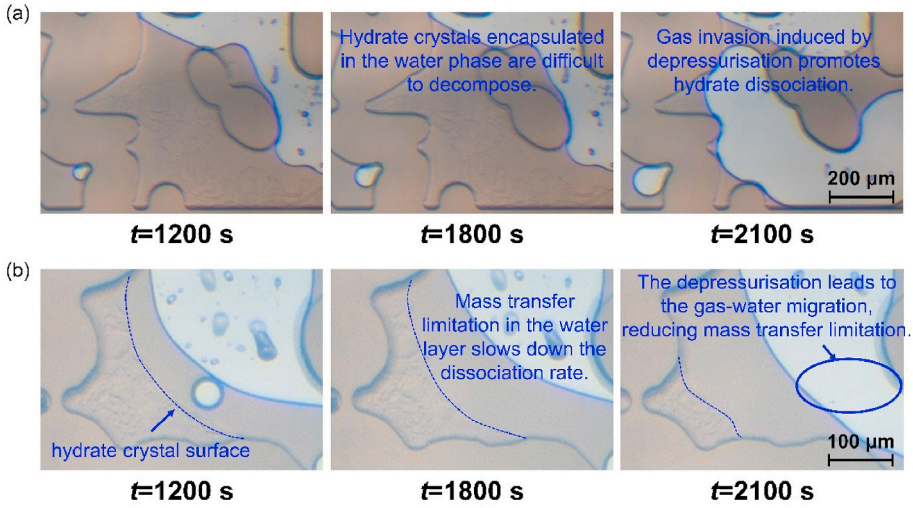

Fig. 8. Local magnification of the experimental snapshot during the slow dissociation stage from Test 3 with a depressurisation rate of 0.4 MPa/15 min.

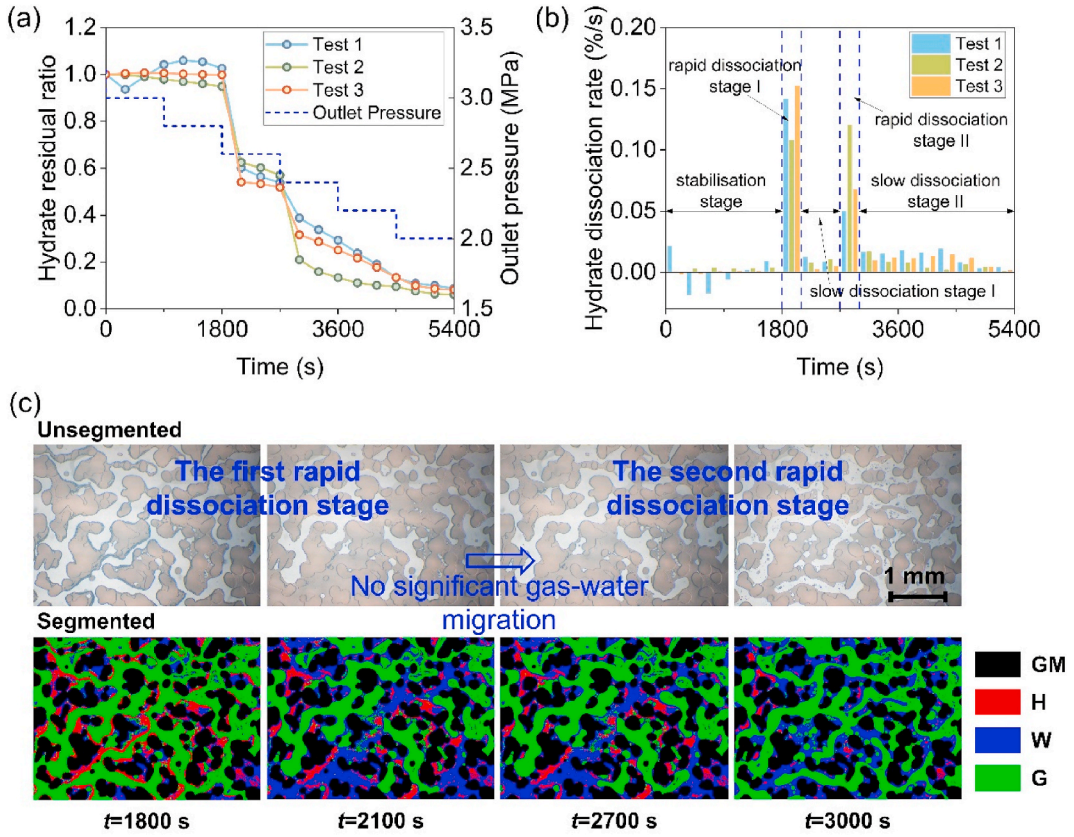

Fig. 9. (a) Hydrate residual rate curves for different experimental tests with the depressurisation rate of 0.2 MPa/15 min. (b) Average hydrate dissociation rate during different time intervals for different experimental tests. (c) Experimental snapshots and segmented images during two rapid dissociation stages from Test 2 at 0.2 MPa/15 min.

As shown in Fig. 9 (b), the entire hydrate dissociation process can be segmented into five stages. Before $t = 1800$ s, with the internal pressure of the chip exceeding 2.8 MPa, the driving force for hydrate dissociation is inadequate, resulting in minimal dissociation and formation of hydrate within the chip. The dissociation is in the stabilisation stage, which is similar to the case of 0.4 MPa/15 min. At $t = 1800$ s, the outlet pressure drops to 2.6 MPa, and the hydrate enters the first rapid dissociation stage, as shown in Fig. 9(b). Although the dissociation rate initially accelerates, it shortly transitions into a slow dissociation stage at $t = 2100$ s. As mentioned earlier, the fundamental reason for the rapid hydrate dissociation stage is the combination of pressure reduction and gas-water migration, in which gas-water migration plays a dominant role. At the depressurisation magnitude of 0.4 MPa, significant gas-water migration facilitates the dissociation of most hydrates near the gas flow channel in a singular rapid dissociation stage. When the depressurisation magnitude is reduced to 0.2 MPa, the extent and duration of gas-water migration decreased. Consequently, the capacity to alleviate the mass transfer limitations of the water phase on the hydrate surface is

reduced, leading to a decrease of approximately 45% in the rate of hydrate dissociation to 0.11%/s during the rapid dissociation stage compared to the case of 0.4 MPa/15 min. Therefore, the proportion of hydrate dissociation decreases.

To elucidate the impact of depressurisation rates on hydrate dissociation, Fig. 10 presents a detailed experimental visualization specifically highlighting the first rapid dissociation phase. At 1800 s, a notable pressure reduction triggers the dissociation of hydrates, accompanied by the formation of a water layer. This layer increases in thickness from 2100 to 2700 s. Prior studies (Yang et al., 2016, 2024b) have identified that this thickening of the water layer introduces substantial mass transfer limitations, which consequently restricts the rate of hydrate dissociation and results in a slower dissociation phase. This contrasts with the observations in Fig. 6, where high depressurisation rates facilitated gas-water migration, effectively dispersing the water layer. Conversely, when the magnitude of depressurisation is lower, the pressure-driven gas-water transport is insufficient to counteract capillary forces, making it challenging to remove the water layer, as depicted in Fig. 10. Consequently, under these conditions, the rate of hydrate dissociation diminishes markedly compared to the scenario with a depressurisation rate of 0.4 MPa/15 min, primarily due to these mass transfer limitations.

Fig. 11 quantitatively depicts the variations in water saturation throughout the depressurisation process in the typical test under different depressuisation rates. As demonstrated in Fig. 11(a), there is an increase in water saturation during the two rapid dissociation stages at a depressurisation rate of 0.2 MPa/15 min. This increase in water saturation is accompanied by an escalation in mass transfer limitations due to the accumulating water layer. Conversely, at a higher depressurisation rate of 0.4 MPa/15 min, robust gas-water migration aids in the partial removal of the water layer, leading to stable water saturation with a slight decreasing trend, as illustrated in Fig. 11(b). Therefore, at higher depressurisation rates, the mass transfer limitation is mitigated, which consequently accelerates the rate of hydrate dissociation during the rapid dissociation phase.

When the rapid dissociation stage I ends, a large amount of hydrate remains in the chip, as shown in Fig. 9(c). Following the first slow dissociation stage, a subsequent depressurisation, as depicted in Fig. 10 with an enlarged view, reinitiates gas-water migration, which significantly enhances further hydrate dissociation. This secondary round of depressurisation not only reduces the pressure further but also diminishes the mass transfer limitation imposed by the water layer,

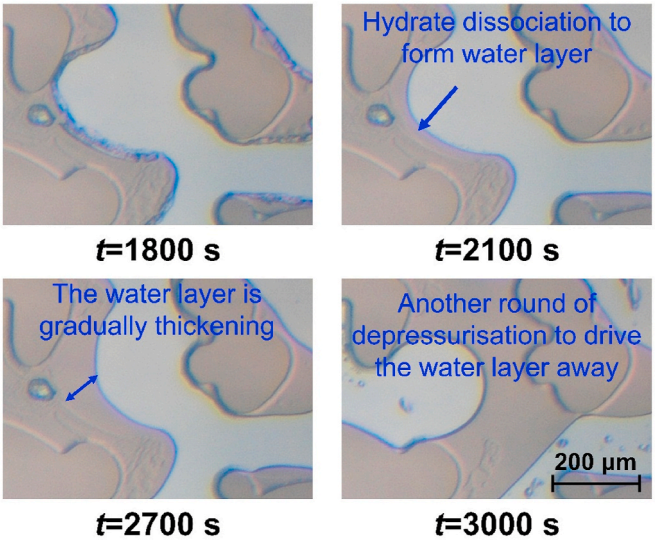

Fig. 10. Local magnification of the experimental snapshot during the first rapid dissociation stage from Test 2 with depressurisation rate of 0.2 MPa/15 min.

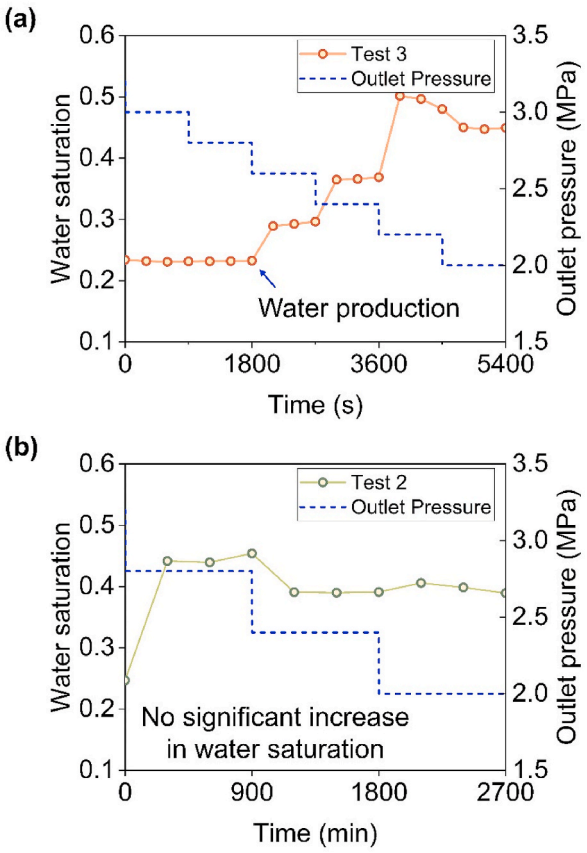

Fig. 11. Typical water saturation curves during deperssurisation at (a) 0.2 MPa/15 min, (b) 0.4 MPa/15 min.

consequently accelerating the rate of hydrate dissociation. This effect is observable at the 3000 s in Fig. 10, where what was initially a slow dissociation of hydrate is rapidly decomposed. The hydrate then enters a second stage of rapid dissociation, where the residual hydrate from the first rapid dissociation stage undergoes further dissociation, as illustrated in Fig. 9(c) at 3000 s, followed by the other slow dissociation stage. The entire rapid dissociation stage is characterised by two segments at the depressurisation rate of 0.2 MPa/15 min.

The experiment demonstrates a distinct behaviour when the rate decreases to 0.1 MPa/15 min. The observed dissociation process unfolds in three stages as shown in Fig. 12(a) and (b). During the stabilisation stage, when the chip pressure remains above the equilibrium threshold, the overall structural integrity of the hydrate is preserved, characterized by minimal dissociation and slight morphological alterations. As the chip pressure continues to drop below the equilibrium pressure after 1800 s, the hydrate begins to undergo slow dissociation with a rate less than 0.07%/s, as shown in Fig. 12(b). Throughout successive depressurisation steps, a consistent pattern of slow dissociation is observed, maintaining uniform rates that are significantly lower than those in the rapid dissociation phase. This phenomenon, termed the uniform dissociation stage, persists until a prolonged duration of 7200 s, culminating in substantial hydrate dissociation and a transition to the slow dissociation phase.

Fig. 12(c) illustrates the experimental images during the uniform dissociation stage in Test 3. Comparative analysis of experimental images at 1800 s and 3600 s reveals minimal gas-water migration within the chip across two depressurisation steps. The majority of the gas-water interface retains its initial positioning, with only fractional water displacement by gas. This limited gas-water transport marginally reduces mass transfer constraints, with the small pressure drops offering minimal dissociation driving force. The release of methane post-

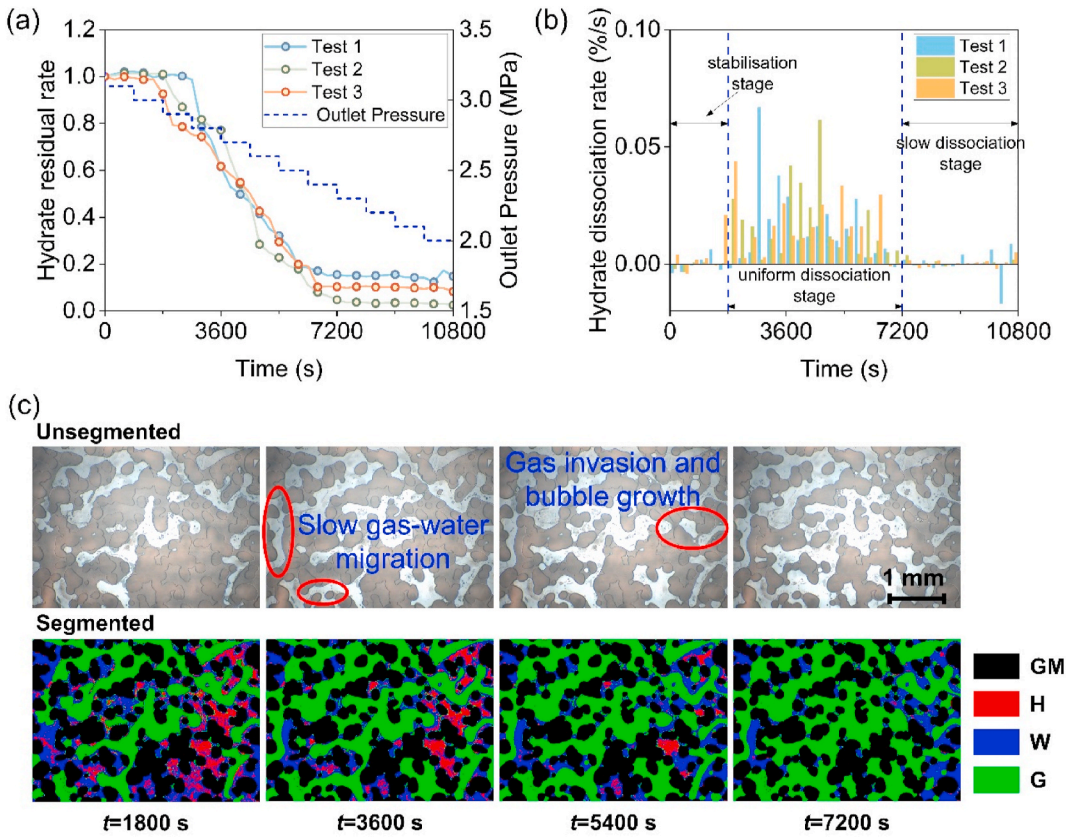

Fig. 12. (a) Hydrate residual rate curves for different experimental tests with the depressurisation rate of 0.1 MPa/15 min. (b) Average hydrate dissociation rate during different time interval for different experimental tests. (c) Experimental snapshots and segmented images during uniform dissociation stages from Test 3 at 0.1 MPa/15 min.

dissociation escalates local fugacity, imposing an additional barrier to further dissociation. This convergence of factors culminates in a subdued dissociation rate. Further examination at 5400 s highlights the emergence of localized bubble growth and gas invasion, attributable to hydrate dissociation. These dissociation-induced gas migrations mildly mitigate the mass transfer limitations in water and enhance the dissociation rate in localized areas. However, the extent and impact of this facilitation are temporally and spatially constrained, insufficient to substantially augment the overall rate of hydrate dissociation. Consequently, as Fig. 10(b) illustrates, the dissociation rate persistently remains low throughout the uniform dissociation stage.

Video S1 provides a comprehensive visualization of the experiment, detailing gas-water migration and hydrate dissociation at a depressurisation rate of 0.1 MPa/15 min. The footage reveals that the gas-water transport is subdued due to the relatively low depressurisation rate. For example, the bubble marked within red circles in the video remain entrapped within the pore structure, immobilized by capillary forces and thus unable to be displaced. This limited gas-water migration does not significantly alleviate the mass transfer limitations imposed by the water layer, as more effectively observed in Fig. 6, resulting in an even slower rate of hydrate dissociation. The slow nature of gas-water migration and hydrate dissociation rates lead to less dramatic phase changes within the pore structure compared to conditions at 0.4 MPa/15 min. In summary, at lower depressurisation rates, the hydrate dissociation process is characterized by a consistently low rate, predominantly due to the slow gas-water migration and insufficient driving forces. However, this slower rate of dissociation results in a smoother and more controllable process, marked by a steady, uniform dissociation rate.

Supplementary video related to this article can be found at https://doi.org/10.1016/j.jgsce.2024.205393

3.3. Implications to hydrate recovery

The above experimental evidence suggests that gas-water migration critically influences hydrate dissociation rates. The displacement of the water phase significantly mitigates mass-transfer limitations, thereby accelerating hydrate dissociation. Consequently, modulating the pressure gradient is essential for managing hydrate dissociation. Firstly, the magnitude of depressurisation in each step dictates the driving force for the dissociation: a greater pressure drop enhances this force, thereby increasing the dissociation rate. Secondly, the depressurisation magnitude influences gas-water migration: a larger pressure drop elevates the gas-water migration rate, leading to the more extensive replacement of water by gas, reduced mass transfer limitations, and higher dissociation rates. Although increasing the depressurisation rate can effectively increase the hydrate dissociation rate (for example, the rate of 0.4 MPa/15 min), in practical engineering, the rapid hydrate dissociation and gas-water migration may lead to the high water production and the instability of reservoir pressure and temperature. This instability can cause issues like leakage and hydrate reformation. In contrast, reducing the depressurisation magnitude, though resulting in a slower dissociation rate, makes the process more stable and controllable. Adjusting the depressurisation rate in actual mining operations depends on specific conditions. In scenarios with high water content in the reservoir and slow hydrate extraction rates, increasing the depressurisation rate can enhance extraction efficiency. Conversely, when reservoir pressure and temperature fluctuations are excessive, decreasing the pressure reduction gradient can render the mining process more stable and manageable.

4. Conclusions

In the present work, we conduct pore-scale experimental investigations into methane hydrate dissociation during stepwise depressurisation using microfluidic chips. The rate of dissociation under varying depressurisation conditions is quantitatively assessed through machine learning-based image segmentation techniques. This approach allows for an in-depth analysis of dissociation characteristics at different depressurisation rates.

A notable observation is the emergence of a distinct three-stage dissociation pattern when subjected to a high depressurisation rate of 0.4 MPa/15 min. Initially, in the stabilisation stage, the hydrate structure remains largely unaltered, exhibiting minimal dissociation or formation due to inadequate thermodynamic driving force and mass transfer limitations. When the pressure drops for another round, the dissociation accelerates, driven by the significant pressure reduction and facilitated by enhanced gas-water migration, which mitigates the impact of mass transfer limitations. Following this rapid dissociation stage, a residual amount of hydrate persists, decomposing slowly as the pressure continues to drop, marking the transition to the slow dissociation stage.

When the depressurisation rate is reduced to 0.2 MPa/15 min, the rapid dissociation stage splits into two discontinuous segments, attributable to the reduced intensity of gas-water migration caused by a lesser pressure drop. This results in a slower dissociation rate. After the first rapid stage, a considerable quantity of hydrate remains, with the cessation of gas-water migration hindering further dissociation. Additional depressurisation is necessary to sustain the gas-water migration and drive the process into the subsequent rapid stage. Further reduction of the depressurisation rate to 0.1 MPa/15 min leads to even slower gas-water migration and insufficient driving force for dissociation. Consequently, the dissociation process is segmented into three stages: stabilisation, uniform dissociation, and slow dissociation. At this lower rate, the dissociation proceeds more slowly but offers enhanced stability and controllability.

This study underscores the profound impact of depressurisation rate on gas-water migration dynamics and, consequently, on the rate of hydrate dissociation. By fine-tuning the magnitude of depressurisation, efficient hydrate extraction can be achieved. These insights offer valuable theoretical underpinnings for the strategic exploitation of hydrates.

CRediT authorship contribution statement

Junyu Yang: Writing – original draft, Visualization, Investigation, Formal analysis, Conceptualization. **Qianghui Xu:** Writing – review & editing, Supervision, Resources, Project administration, Investigation, Funding acquisition, Data curation, Conceptualization. **Boyu Huang:** Writing – review & editing, Visualization, Validation, Methodology, Investigation, Formal analysis, Conceptualization. **Yizhe Liu:** Writing – review & editing, Visualization, Validation, Investigation, Formal analysis, Data curation, Conceptualization. **Zhiying Liu:** Writing – review & editing, Validation, Investigation, Conceptualization. **Le Zhang:** Conceptualization, Resources, Writing – review & editing. **Kai H. Luo:** Writing – review & editing, Supervision, Project administration, Funding acquisition. **Lin Shi:** Supervision, Project administration, Funding acquisition.

Declaration of competing interest

The authors declare that they have no known competing financial interests or personal relationships that could have appeared to influence the work reported in this paper.

Data availability

Data will be made available on request.

Acknowledgements

This work is supported by the National Natural Science Foundation of China (No. 52206014 & 51876100 & 52236003). Additional support from the UK Engineering and Physical Sciences Research Council (EPSRC) under the grant Nos. EP/W026260/1 and EP/X035875/1 is also acknowledged.

Appendix A. Supplementary data

Supplementary data to this article can be found online at https://doi.org/10.1016/j.jgsce.2024.205393.

References

Almenningen, S., Iden, E., Fernø, M.A., Ersland, G., 2018. Salinity effects on pore-scale methane gas hydrate dissociation. J. Geophys. Res. Solid Earth 123, 5599–5608.
Anderson, B.J., Kurihara, M., White, M.D., Moridis, G.J., Wilson, S.J., Pooladi-Darvish, M., Gaddipati, M., Masuda, Y., Collett, T.S., Hunter, R.B., Narita, H., Rose, K., Boswell, R., 2011. Regional long-term production modeling from a single well test, mount Elbert gas hydrate stratigraphic test well, Alaska North Slope. Mar. Petrol. Geol. 28, 493–501.
Berg, S., Kutra, D., Kroeger, T., Straehle, C.N., Kausler, B.X., Haubold, C., Schiegg, M., Ales, J., Beier, T., Rudy, M., Eren, K., Cervantes, J.I., Xu, B., Beuttenmueller, F., Wolny, A., Zhang, C., Koethe, U., Hamprecht, F.A., Kreshuk, A., 2019. ilastik: interactive machine learning for (bio)image analysis. Nat. Methods 16, 1226–1232.
Chen, L., Feng, Y., Kogawa, T., Okajima, J., Komiya, A., Maruyama, S., 2018. Construction and simulation of reservoir scale layered model for production and utilization of methane hydrate: the case of Nankai Trough Japan. Energy 143, 128–140.
Egorov, A.V., Nigmatulin, R.I., Rozhkov, A.N., 2016. Heat and mass transfer effects during displacement of deepwater methane hydrate to the surface of Lake Baikal. Geo Mar. Lett. 36, 215–222.
Gao, Q., Yin, Z., Zhao, J., Yang, D., Linga, P., 2021. Tuning the fluid production behaviour of hydrate-bearing sediments by multi-stage depressurization. Chem. Eng. J. 406.
Ge, K., Zhang, X., Wang, J., Cheng, C., He, J., 2023. Optimization of the depressurization rate and stepwise strategy for hydrate exploitation using a genetic algorithm-based depressurization method. Chem. Eng. Sci. 265, 118218.
Ji, C., Ahmadi, G., Smith, D.H., 2001. Natural gas production from hydrate decomposition by depressurization. Chem. Eng. Sci. 56, 5801–5814.
Kan, J., Sun, Y., Dong, B., Yuan, Q., Liu, B., Sun, C., Chen, G., 2021. Numerical simulation of gas production from permafrost hydrate deposits enhanced with CO2/N2 injection. Energy 221, 119919.
Katsuki, D., Ohmura, R., Ebinuma, T., Narita, H., 2007. Methane hydrate crystal growth in a porous medium filled with methane-saturated liquid water. Phil. Mag. 87, 1057–1069.
Kim, H., Bishnoi, P.R., Heidemann, R.A., Rizvi, S.S., 1987. Kinetics of methane hydrate decomposition. Chem. Eng. Sci. 42, 1645–1653.
Kurihara, M., Sato, A., Funatsu, K., Ouchi, H., Yamamoto, K., Numasawa, M., Ebinuma, T., Narita, H., Masuda, Y., Dallimore, S.R., 2010. Analysis of production data for 2007/2008 Mallik gas hydrate production tests in Canada. In: International Oil and Gas Conference and Exhibition in China. OnePetro.
Li, X., Liu, M., Li, Q., Pang, W., Chen, G., Sun, C., 2023. Visual study on methane hydrate formation and depressurization-induced methane hydrate dissociation processes in a micro-packed bed reactor. Fuel 332, 125980.
Liu, L., Shao, H., Fu, S., Wu, N., 2016. Theoretical simulation of the evolution of methane hydrates in the case of Northern South China Sea since the last glacial maximum. Environ. Earth Sci. 75.
Mok, J., Choi, W., Lee, J., Seo, Y., 2022. Effects of pressure and temperature conditions on thermodynamic and kinetic guest exchange behaviors of CH4 − CO2 + N2 replacement for energy recovery and greenhouse gas storage. Energy 239, 122153.
Pandey, J.S., Almenningen, S., von Solms, N., Ersland, G., 2021. Pore-scale visualization of CH4 gas hydrate dissociation under permafrost conditions. Energy Fuel. 35, 1178–1196.
Pang, W.X., Xu, W.Y., Sun, C.Y., Zhang, C.L., Chen, G.J., 2009. Methane hydrate dissociation experiment in a middle-sized quiescent reactor using thermal method. Fuel 88, 497–503.
Sloan, E.D., 1998. Gas hydrates: review of physical/chemical properties. Energy Fuel. 12, 191–196.
Sloan, E.D., 2003. Fundamental principles and applications of natural gas hydrates. Nature 426, 353–359.
Tohidi, B., Anderson, R., Clennell, M.B., Burgass, R.W., Biderkab, A.B., 2001. Visual observation of gas-hydrate formation and dissociation in synthetic porous media by means of glass micromodels. Geology 29, 867–870.
Wang, B., Fan, Z., Wang, P., Liu, Y., Zhao, J., Song, Y., 2018. Analysis of depressurization mode on gas recovery from methane hydrate deposits and the concomitant ice generation. Appl. Energy 227, 624–633.
Wei, J., Fang, Y., Lu, H., Lu, H., Lu, J., Liang, J., Yang, S., 2018. Distribution and characteristics of natural gas hydrates in the Shenhu sea area, south China sea. Mar. Petrol. Geol. 98, 622–628.

Yamamoto, K., Wang, X.X., Tamaki, M., Suzuki, K., 2019. The second offshore production of methane hydrate in the Nankai Trough and gas production behavior from a heterogeneous methane hydrate reservoir. RSC Adv. 9, 25987–26013.
Yang, L., Falenty, A., Chaouachi, M., Haberthür, D., Kuhs, W.F., 2016. Synchrotron X-ray computed microtomography study on gas hydrate decomposition in a sedimentary matrix. G-cubed 17, 3717–3732.
Yang, M., Zhao, J., Zheng, J.-n., Song, Y., 2019. Hydrate reformation characteristics in natural gas hydrate dissociation process: a review. Appl. Energy 256, 113878.
Yang, J., Xu, Q., Liu, Z., Shi, L., Lei, T., Luo, K.H., 2023. Upscaling methane hydrate dissociation kinetic model during depressurisation. Chem. Eng. Sci. 275, 118742.
Yang, J., Xu, Q., Kou, X., Wang, G., Lei, T., Wang, Y., Li, X., Luo, K.H., 2024a. Three-dimensional pore-scale study of methane hydrate dissociation mechanisms based on micro-CT images. The Innovation Energy 1, 100015.
Yang, J., Liu, Y., Xu, Q., Liu, Z., Dai, X., Shi, L., Luo, K.H., 2024b. Pore-scale visualization of hydrate dissociation and mass transfer during depressurization using microfluidic experiments. Fuel 368, 131519.
Yuan, Q., Sun, C., Yang, X., Ma, P., Ma, Z., Li, Q., Chen, G., 2011. Gas production from methane-hydrate-bearing sands by ethylene glycol injection using a three-dimensional reactor. Energy Fuel. 25, 3108–3115.